Food Hydrocolloids 155 (2024) 110121

Contents lists available at ScienceDirect

Food Hydrocolloids

journal homepage: www.elsevier.com/locate/foodhyd

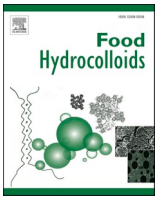

SANS and SAXS: A Love Story to unravel structural evolution of soy proteins and polysaccharide fibres during high moisture extrusion for meat alternatives

Ekaterina D. Garina [a], Ruud den Adel [b], John P.M. van Duynhoven [b,c], Gregory N. Smith [d], Robert M. Dalgliesh [d], Michael Sztucki [e], Wim G. Bouwman [a,*]

[a] Department of Radiation Science and Technology, Delft University of Technology, Mekelweg 15, 2629 JB, Delft, the Netherlands
[b] Unilever Global Foods Innovation Centre, Bronland 14, 6708 WH, Wageningen, the Netherlands
[c] Laboratory of Biophysics, Wageningen University and Research, Stippeneng 4, 6708WE, Wageningen, the Netherlands
[d] ISIS Neutron and Muon Source, Science and Technology Facilities Council, Rutherford Appleton Laboratory, Chilton, Oxon, OX11 0QX, UK
[e] ESRF, The European Synchrotron Radiation Facility, 71 Avenue des Martyrs, CS40220, 38043, Grenoble, Cedex 9, France

ARTICLE INFO

Original content: Effects of pH and salt concentration on the fibrous structure formation of plant proteins during high-moisture extrusion and shear (Original data)
Structure formation and structure evolution during high moisture extrusion of soy proteins (Original data)

Keywords:
Soy proteins
Structure formation
High-moisture extrusion
Small-angle scattering (SAS)

ABSTRACT

Plant-based meat alternatives are seeing considerable interest due to their potential to reduce environmental burden and enhance population health. The food industry, therefore, seeks routes to provide the consumer with whole-cut plant-based products that closely resemble meat products. High-moisture extrusion (HME) of plant proteins enables the industrial manufacturing of meat-like products with highly hierarchical structural organisation of fibres. The major bottleneck in serving the growing market for these products is a lack of insight into how multiscale structures evolve during shear processing. Furthermore, it remains an open question of how two biopolymers, one being a plant protein and the other being a polysaccharide, contribute to the anisotropic structure formation during HME. This study shows how the complementary use of small-angle neutron scattering (SANS) and small-angle X-ray scattering (SAXS) can add clarity to these matters, benefiting from the different contrasts in scattering length density (SLD) encountered with each of these methods. It is demonstrated that two biopolymers have differences in the development of structural anisotropy. The protein fibril alignment starts in the extruder section with its further development along the cooling die. On the other hand, for polysaccharide fibres, the strongest local alignment has been found in the transition zone.

1. Introduction

Even though animal agriculture has been proven to be a major contributor to climate change (Aiking and de Boer, 2020), meat is still a food staple in a population's diet. One barrier to reducing the consumption of animal products is consumer habits (van den Berg, van den Brink, Wagemakers, & den Broeder, 2022). Meat is often described as having a unique sensory profile, being comforting and familiar (Collier et al., 2021). The unique textural properties of animal meat are a result of the highly hierarchical structural organisation of fibres that is not trivial to replicate (Pette & Staron, 1990). The food industry, therefore, seeks routes to provide the consumer with whole-cut plant-based products that closely resemble meat.

The technological routes most amenable for industrial implementation rely on shear processing through high-moisture extrusion (HME) (40–80 % [w/w] water) (Akdogan, 1999). The process includes a mixing and hydration step, thermo-mechanical treatment, and a cooling step (Cornet et al., 2022). The final step is commonly seen as a requirement for the formation of the characteristic anisotropic structure.

In HME, plant proteins and polysaccharides are typically mixed to create meat alternatives. Although recent research suggests that using a second biopolymer is not a prerequisite for anisotropic structure formation (Wittek, Zeiler, Karbstein, & Emin, 2021b; Osen, Toelstede, Wild, Eisner, & Schweiggert-Weisz, 2014), the additional biopolymer phase is thought to improve texture by enhancing fracturing during eating (van der Sman & van der Goot, 2023). That is why, besides price considerations, the food industry commonly employs protein concentrates that are less refined than protein isolates. The concentrates

* Corresponding author.
E-mail address: W.G.Bouwman@tudelft.nl (W.G. Bouwman).

https://doi.org/10.1016/j.foodhyd.2024.110121
Received 24 January 2024; Received in revised form 10 April 2024; Accepted 18 April 2024
Available online 3 May 2024

additionally contain polysaccharides, mainly originating from cell wall fragments, composed of semi-crystalline cellulose embedded into the matrix of hemicellulose and pectin.

Despite the extensive research suggesting hypotheses for the formation and evolution of structure during extrusion (Wittek, Zeiler, Karbstein, & Emin, 2021c; Ubbink & Muhialdin, 2022; Schmid, Farahnaky, Adhikari, & Torley, 2022; Guyony, Fayolle, & Jury, 2023; van der Sman & van der Goot, 2023), the field is still at an exploratory stage. Empirical knowledge dominates the control and design of this process, making the actual HME process a black box (Emin & Schuchmann, 2017). The reason for this lies in the inherent difficulty of studying these hierarchically assembled multicomponent systems alongside the substantial heterogeneity of their structures. The complex hierarchical architecture of extrudates necessitates the use of multiple characterisation techniques in order to elucidate the mechanism by which two biopolymers, one being a plant protein and the other being a polysaccharide, contribute to the structure formation. In this context, the combination of small-angle neutron scattering (SANS) with small-angle X-ray scattering (SAXS) appears to be an efficient strategy for studying the role of both proteins and polysaccharide fibres in the anisotropic structure formation from the nano-to submicron scale. Several studies have already utilised the capabilities of SANS (Tian et al., 2020) and SAXS (Goh et al., 2005; Zink et al., 2024) to gain insights into the anisotropic structure of a product featuring a hierarchical structural arrangement of fibres. In this study, the different contrasts in scattering length density (SLD) between the different components with respect to water for neutrons and X-rays unravel the nanostructural evolution of soy proteins and polysaccharide fibres during HME by studying materials collected from different zones in the extruder barrel and cooling die upon a dead-stop operation.

2. Materials and methods

2.1. Materials

Commercial soy protein concentrate (SPC, Alpha 8® IP, 96% DM with 70% in dry base, 2% fat, 7% ash, 18% dietary fibre, and total carbohydrates of 19.6%) from Solae (St. Louis, MO, USA) was used in this work.

The fibre composition of the SPC was determined by quantitative NMR. The analysis showed the presence of a small amount of free sugars (sucrose, stachyose); most sugars were present as polysaccharides. The monosaccharide composition, upon Saeman hydrolysis, showed a strong contribution of glucose, pointing to cellulose. The other monosaccharides (galacturonic acid, galactose, arabinose, mannose, rhamnose, xylose) pointed to pectin and hemicellulose that were embedded in the fibre (cell wall) matrix. The detailed fibre composition of SPC is demonstrated in Table S1.

2.2. Extrusion processing

Extrusion trials were performed using a co-rotating twin-screw extruder (XTS 19, Xtrutech, UK) with a screw diameter of 19 mm and length-to-diameter (L/D) ratio of 25. A rectangular cooling die (17 mm (width) x 7 mm (height) x 300 mm (length)) was coupled to the extruder through a die adapter. A breaker plate was placed before the cooling die.

The extruder barrel was segmented into four temperature-controlled zones that were electrically heated and cooled with water-cooling inserts inside the barrel. The temperature in the cooling die was regulated by tap water functioning as a cooling medium. The dry protein concentrate was fed into the extruder with a volumetric feeder (Brabender Technologie, Utrecht, Netherlands). Water was injected via an inlet channel with the use of a constant-flow pump (Master Flex Easy Load II, USA).

The extrusion trials were run at the screw speed of 350 rpm and moisture content of ca. 54%. The barrel temperatures were set at 80 °C, 120 °C, 160 °C, and 135 °C in zones 1 to 4. The die temperature was set at 135 °C. The cooling was maintained at a temperature of 65 °C. Extrudate samples were collected from the cooling die outlet after reaching a steady state, as indicated by constant process responses. The samples were immediately frozen and stored at −18 °C.

For the dead-stop operation, the extrusion process was deliberately stopped after collecting the extrudates. The extruder barrel section was cooled using the maximum cooling capacity, and the screws were stopped. The temperature of the cooling water was lowered to ambient temperature. Cold water was immediately poured on the extruder barrel and die sections to ensure efficient machine cooling (for the small-scale extruder, the expected time for the contents of the barrel and cooling die to reach ambient temperature is less than a minute). The die adaptor and the cooling die were disassembled from the extruder, and the ribbon was expelled from the cooling die by applying water pressure. After the dead-stop, samples were also taken from screw, transition and die zones. The dead-stop operation was carried out twice to obtain a sufficient number of samples. All the collected dead-stop samples were immediately frozen and stored at −18 °C. A schematic diagram of HME and sampling procedure is presented in Fig. 1A.

2.3. Slice preparation for Small-Angle Scattering (SAS)

A schematic diagram of the slice preparation procedure for Small-Angle Scattering measurements is displayed in Fig. 1B. The samples were sliced at a thickness of 500 μm using a cryo-microtome (Cryostar NX70, Thermo Fisher Scientific, Germany), which ensured high precision cutting (section thickness range is 0.5–500 μm). The sectioning was performed at the specimen head and blade temperatures of −12 °C and −10 °C, respectively. The bonding of the samples to the specimen holder was ensured by embedding the materials into the Tissue-Tek® O·C.T. Compound (Sakura Finetek, USA) embedding medium. In order to account for the existing temperature gradient in the cooling die (Wittek, Ellwanger, Karbstein, & Emin, 2021a), skin and core slices were obtained for extrudate and dead-stop ribbon samples. Only one slice was made for dead stops taken from the screw, transition, and non-cooled die zones. The acquired slices were sandwiched between microscope slides covered with Ultralene thin film (Spex® SamplePrep, USA) and subsequently sealed. This was to ensure the stability of the product during its further storage (at −18 °C). Note that the slides and Ultralene film were removed for following SAS measurements. Additional extrudate skin slices intended for contrast variation SANS experiments (subsubsection 3.1.1) were taken manually with a scalpel knife, which affected the accuracy of thickness determination.

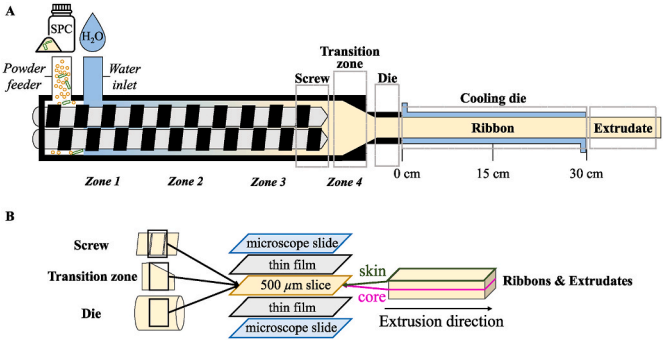

Fig. 1. (A) Schematic diagram of HME. Sampling positions are represented by grey rectangles. Yellow dots and green cylinders represent protein and polysaccharide fibres components of SPC powder, respectively. (B) Schematic diagram of slices preparation procedure for SAS measurements. The figure is not to scale.

2.4. Small-angle neutron scattering (SANS)

2.4.1. Preparation of soy protein concentrate doughs

To ensure different contrast conditions with SANS, water mixtures of different H_2O/D_2O compositions were prepared. SPC doughs were obtained by adding SPC powder to the water mixtures at ca. 54%, w/w, total solids. The doughs were manually mixed using a spatula and stored at room temperature (20 °C) for at least 12 h before SANS measurements. This procedure was intended to mimic the 'starting conditions' of HME during the mixing and hydration step.

2.4.2. SANS experimental procedure

SANS measurements were performed on the Larmor Instrument at the ISIS Neutron and Muon Source (STFC Rutherford Appleton Laboratory, UK) (ISIS Larmor). The time-of-flight setup at ISIS allowed a simultaneous Q range of 0.005–0.7 $Å^{-1}$ by utilising an incident wavelength range of 0.9–13 Å. Q is the magnitude of the scattering angle defined as:

$$Q = \frac{4\pi}{\lambda}\sin\theta \tag{1}$$

where 2θ is the scattering angle, and λ is the incident neutron wavelength.

Due to the anisotropic nature of the samples, the instrument was configured with the symmetric squared sample aperture (6 × 6 mm^2). SPC doughs, extrudates, and dead-stop samples were loaded into gel cell sample holders with demountable quartz windows to ensure an air-tight environment during the measurements. To enable different contrasts in SLD, manually sliced extrudate skin samples were soaked in D_2O or H_2O/D_2O mixtures for at least 24 h before being transferred to the holders (note that manual slicing procedure was performed only for contrast variation experiments, all 'natural' contrast experiments were carried out with the sliced prepared according to subsection 2.3). Independent neutron radiography measurements were carried out at FISH, a thermal neutron imaging station in Delft (Zhou et al., 2018), to ensure that the soaking time of 24 h is enough to allow the samples to come to equilibrium. It should be noted that the swelling of extrudates does not affect the overall multiscale structure and can be adequately described by the Flory–Rehner theory of crosslinked polymer networks (Cornet, Snel, Lesschen, van der Goot, & van der Sman, 2021). During the measurements, extrudate and dead-stop samples were mounted with the specific rotation angle, φ_0. The rotation angle was aimed at 45° to exclude the possibility that anisotropic aberrations of the instrument in horizontal and vertical directions would have an effect on the retrieved anisotropy parameters. A schematic of sample placement and measurement strategy is shown in Fig. 2A.

2.4.3. SANS data analysis

All two-dimensional (2D) scattering data were reduced using the instrument-specific software Mantid (Arnold et al., 2014). By selecting several wavelength bands in the data reduction, it was checked that there were no multiple scattering effects present in the measurements. The raw data were placed on an absolute scale (cm^{-1}) by measuring the scattering of a mixture of hydrogenous and deuterated polystyrene with a known radius of gyration and scattering cross-section (Wignall & Bates, 1987). The data were corrected for detector sensitivity. The scattering background of the quartz windows was subtracted. Isotropic 2D SANS patterns were radially averaged to obtain one-dimensional (1D) scattering profiles, $I(Q)$. When 2D SANS data displayed anisotropy, the sector averages of the width of ±15° were taken parallel (∥) and perpendicular (⊥) to the alignment direction.

SasView software (Doucet et al., 2022) was utilised to fit radial and sector averages using the Levenberg-Marquardt algorithm (Levenberg, 1944; Marquardt, 1963), the standard method for non-linear data fitting. Different phenomenological models, such as a generalised anisotropic Guinier-Porod model previously used to quantify the hierarchical structure in fibrous calcium caseinate (Tian et al., 2020), a model consisting of the sum of a power-law term plus Guinier-Porod model (Hammouda, 2010), and a broad peak model Tian et al. (2020) were considered to fit the scattering data. However, only the broad peak model provided a good fit to the scattering data. The shape-independent empirical broad peak model is given by:

$$I(Q) = \frac{A}{Q^n} + \frac{C}{1 + (|Q - Q_0|\xi)^m} + B \tag{2}$$

where A is the power-law scale factor, n is the power-law exponent, C is

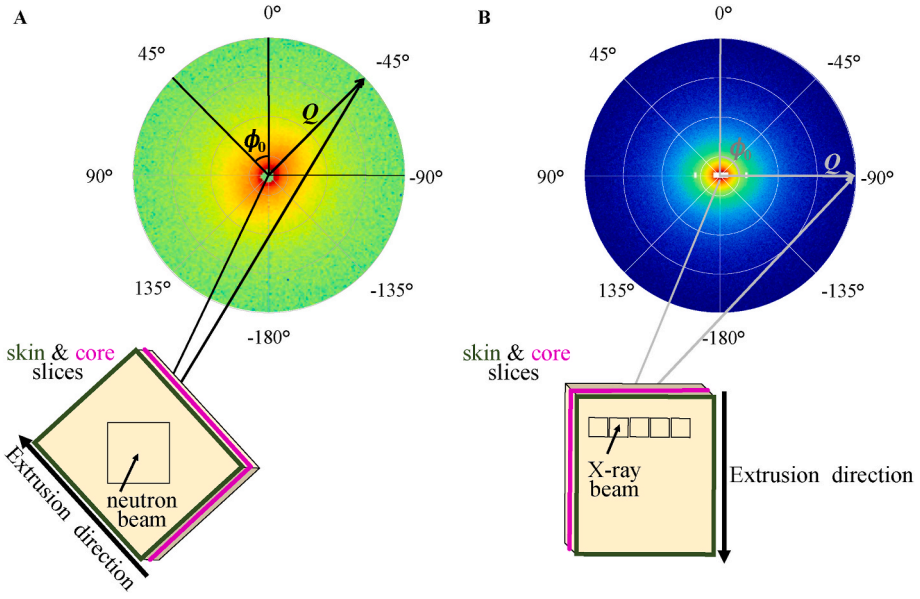

Fig. 2. (A) Schematic diagram of sample placement with respect to a neutron beam and a typical two-dimensional SANS pattern. The specific rotation angle, φ_0, was intended to be ca. −45° throughout the measurements. (B) Schematic diagram of sample placement with respect to an X-ray beam and a typical two-dimensional (U) SAXS pattern. Samples were placed perpendicularly to the extrusion direction. Thus, for the ribbons, the specific rotation angle, φ_0, was intended to be ca. 90°. For the dead-stops collected from the extruder section, φ_0 vary from 0° to 180° depending on the sampling position. The figure is not to scale.

the Lorentzian scale factor, ξ is the Lorentzian correlation length, m is the exponent of Lorentz function, B is the flat background that accounts for incoherent scattering from the hydrogenous material. Q_0 is the peak position related to the characteristic centre-to-centre distance (D) between the scattering inhomogeneities, where $D = 2\pi/Q_0$.

Compared to shape-dependent models, applying the broad peak model is less likely to lead to overfitting the data due to the lower number of fitting parameters. It is not possible to describe the meat alternatives, which are complex multiphase and polydisperse systems with shape-dependent models. These models will need a much larger number of fitting parameters, which will lead to unrealistic interpretations of the scattering data.

Additionally, insights into the nanostructure anisotropy were gathered from the examination of the annular intensity averages. The averaging of 2D SANS data was carried over a narrow Q range of $Q_{\min} < Q < Q_{trans}$, where $Q_{\min}$ corresponds to the lowest accessible scattering vector to probe the largest possible dimensions of the scatterers, and Q_{trans} corresponds to the transition from isotropic to anisotropic structure. The obtained annular intensity averages were fitted with a Legendre series expansion as described in (Burger, Hsiao, & Chu, 2010):

$$I(Q,\varphi) = \sum_{n=0}^{\infty} a_n P_{2n}(\cos\varphi^*) \tag{3}$$

where $\varphi^* = \varphi - (\varphi_0) + \frac{\pi}{2}$, φ_0 is the orientation angle, a are fitting coefficients, and P_{2n} are even Legendre polynomials. From Equation (3), the nematic order parameter, $\overline{P_2}$, was determined as:

$$\overline{P_2} = \frac{a_1}{5a_0} \tag{4}$$

The value of $\overline{P_2}$ describes the extent of nano-alignment around a certain orientation angle, φ_0. The closer it is to zero, the more isotropic the sample is. The maximum value of the order parameter is determined by the scattering characteristics of a perfectly oriented structure.

2.5. (Ultra-)Small-angle X-ray scattering ((U)SAXS)

2.5.1. (U)SAXS experimental procedure

SAXS and USAXS measurements were performed on the upgraded beamline ID02 of the European Synchrotron Radiation Facility (ESRF, Grenoble, France) (Narayanan et al., 2022). A long evacuated detector tube allowed an automated change of the sample-to-detector distance (SDD) from 1 to 30.9 m, making it possible to collect SAXS and USAXS data with the same setup. For this study, three SDDs (1, 8, and 30.9 m) were used to cover a Q range of 0.0002–0.8 Å^{-1} with an X-ray wavelength of 1.014 Å.

Extrudate and dead-stop slices were mounted on the sample holder. Subsequently, the holder was covered with an Ultralene film, which was sealed with double-sided tape. This provided an air-tight environment and only two layers of film contributed to the background. The small beam size of 100 × 150 μm^2 (v x h) permitted the recording of 20 measurement frames over a range of 8 mm in the direction perpendicular to the extrusion direction (Fig. 2B).

2.5.2. (U)SAXS data analysis

All 2D scattering data were reduced and normalised to an absolute scale (cm^{-1}) using standard procedures (Narayanan et al., 2022). The instrument-specific software SAXSutilities (Sztucki, 2021) was used for scattering background subtraction of the Ultralene film, merging measurements recorded at different SDDs and other specific operations.

In order to account for material heterogeneity, averaging was performed according to the scheme displayed in Fig. 3. It was investigated if the merged intensity curves displayed characteristic shoulder-like features or obeyed a power-law at some Q regions.

As for the SANS data, insights into the nanostructure anisotropy were gathered from the examination of the annular intensity averages. The

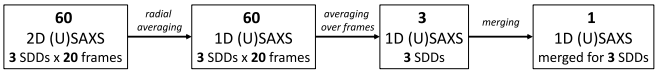

Fig. 3. Scheme of averaging procedure of (U)SAXS data.

annular intensity averages, $I(\varphi)$, were obtained for each measurement frame. The averaging was carried over a Q range of $0.025 > Q > 0.0002$ Å^{-1} (i.e. at SDD of 30.9 m), where anisotropy was best observable. The obtained annular intensity averages were fitted $I(\varphi)$ with a Legendre series expansion as described above. To enable the comparison of different samples under conditions of material heterogeneity, the order parameter and orientation angle values were averaged over 20 measurement frames.

3. Results and discussion

3.1. Small-angle neutron scattering (SANS)

3.1.1. Contrast variation in SPC doughs and extrudates

It is worth clarifying that most measurements described in this work were carried out with food-grade materials produced with tap water and collected directly from the extruder to have the most realistic samples. However, some samples, namely SPC dough and extrudates, were additionally prepared with water mixtures of different H_2O/D_2O compositions as described in subsubsection 2.4.1 and subsubsection 2.4.2. This was intended to elucidate the contribution of the soy proteins and polysaccharide fibres to the scattering. In this work, polysaccharide fibres mainly comprise semi-crystalline cellulose in which pectin and hemicellulose are embedded. Hence, 'polysaccharide fibres' represent the whole, and the word 'cellulose' is used as a 'pars pro toto', 'part representing whole'. Thus, this subsection presents the results for the samples prepared with 'natural' contrast (i.e. with 100% H_2O) and with water mixtures of the following composition: 100% D_2O, 35% D_2O, 42.5% D_2O.

As can be seen from Table 1, the neutron SLD difference (Neutron $SLD_{proteins}$ - Neutron SLD_{H_2O}) between proteins and H_2O is only marginally greater than the difference between cellulose and H_2O ($SLD_{cellulose}$ - Neutron SLD_{H_2O}). However, given the low mass fraction of cellulose compared to that of proteins, it is reasonable to assume that in 'natural' contrast SANS experiments, the greater contribution to scattering is due to proteins. Nevertheless, it must be emphasised that the contribution of cellulose to the neutron scattering intensities cannot be completely eliminated, as evidenced by the variations in scattering intensities from the doughs of SPC and soy protein isolate (SPI) (cellulose content in SPI is negligible) (Fig. S1). As for the other H_2O/D_2O compositions, it is expected that around 42.5% D_2O soy proteins will be contrast-matched, making the scattering contrast arise primarily from the SLD difference of cellulose relative to water. Around 35% D_2O, the scattering signal is anticipated to be due to the contrast between proteins

Table 1
Theoretical neutron and X-ray SLDs for soy proteins, semi-crystalline cellulose (Martínez-Sanz, Gidley, & Gilbert, 2015), H_2O and D_2O. The SLDs of soy proteins were estimated with the SLD calculator on the website of the National Institute of Standards and Technology (NIST) (NIST). For these calculations, the empirical formula of soy proteins was determined to be $C_{12}H_{12}N_2O_3$ and the mass density of 1.3 g/cm^3 was used (ChemSrc).

	Neutron SLD (10^{10} cm^{-2})	X-Ray SLD (10^{10} cm^{-2})
Soy Proteins	2.39	11.63
Cellulose (crystalline)	1.87	14.46
Cellulose (amorphous)	1.73	13.38
H_2O	−0.56	9.47
D_2O	6.34	9.43

Contrast match point for soy proteins: 42.5% D_2O Contrast match point for crystalline cellulose: 35% D_2O.

and water. With 100% D_2O, the highest intensity of the scattering data is expected due to the greatest contrast with respect to soy proteins and/or cellulose.

At a temperature below the melting (denaturation) temperature(s) of the biopolymers, the dough is expected to be a random, isotropic mixture in which immiscible biopolymers remain in separate phases. As expected, SANS patterns of the unprocessed SPC doughs were found to be isotropic. Thus, they were radially averaged to obtain $I(Q)$ plots presented in Fig. 4. In general, incoherent background scattering arising from the hydrogenous material is predominant at the high Q region ($Q > 0.07$ Å^{-1}). This is less pronounced for SPC dough in 100% D_2O due to the substitution of hydrogen for deuterium. The similarity in the incoherent background levels between 100% H_2O, 35% D_2O, and 42.5% D_2O is most likely caused by the nonuniform distribution of the dough samples in the gel cell sample holders (due to the 'crumbly' texture of the doughs), which affected the absolute intensities. Furthermore, it should also be clarified that, in general, one does not expect a clear scaling effect of the incoherent background with the amount of D_2O due to the fact that only part of the background is due to water; the rest is due to hydrogens constituting nearly half of the atoms in proteins and polysaccharides. Nevertheless, the highest intensity of the scattering data is observed for the 100% D_2O sample, and the lowest contrast is provided by the doughs prepared with D_2O/H_2O mixtures. For all doughs, scattering at low Q ($Q <$ ca. 0.01 Å^{-1}) is dominated by power-law behaviour, suggesting the presence of larger structures and/or aggregate formation. An increase in scattering intensities at the low Q region was also demonstrated for SPI dough (Fig. S1), implying that soy proteins are responsible for this observation. In Tian et al. (2020), similar low Q behaviour in the scattering data from unsheared caseinate protein dispersion was also attributed to the presence of larger aggregates or clusters of sub-aggregates in the protein gel. Although the cited work examines a different protein system, the observed scattering behaviour is fairly similar to scattering from SPC systems. However, in the case of SPC dough, cellulose chains could additionally contribute to the low Q behaviour. For 100% H_2O and 100% D_2O SPC doughs, this power-law region is followed by a distinctive shoulder in the Q range between ca. 0.01 and 0.08 Å^{-1}. In Tian et al. (2020), a similar shoulder feature was attributed to the sub-aggregate structure of the protein dispersion. Due to the lowered overall contrast and reduced scattering intensities in the 35% D_2O and 42.5% D_2O SPC doughs, poor shoulder resolution is inherent to these samples.

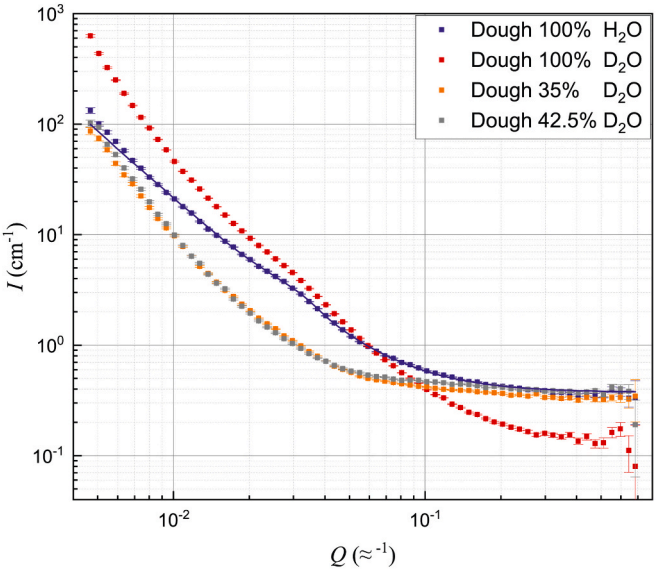

Fig. 4. Radially averaged SANS data from SPC doughs prepared with 54% w/w moisture content for different H_2O/D_2O compositions. Square symbols represent the experimental data and the line represents the fit with the broad peak model to the 100% H_2O dough SANS data.

Similar observations were made for extruded soy proteins, unsoaked and soaked in mixtures of different H_2O/D_2O compositions Fig. 5. Since HME induces anisotropic structure formation, the circular symmetric radial averaging, performed to generate 1D plots presented in Fig. 4, is no longer valid. Sector averages should be taken in the directions parallel and perpendicular to the orientation direction. Fig. 5 displays 2D SANS data and corresponding sector intensities for extrudate skin slices. As for protein doughs (Fig. 4), the greatest contrast is provided by the sample soaked in 100% D_2O and the lowest scattering intensities are observed for extrudates soaked in H_2O/D_2O mixtures. Apparently, the difference in the incoherent background levels between 100% H_2O extrudate and extrudates soaked in 35% and 42.5% D_2O is more obvious compared to the dough samples as a result of increased certainty regarding slice thicknesses. However, it should be noted that for extrudate slices, it is also not possible to completely eliminate the chance of some uncertainty in sample thickness determination due to manual slicing of these samples. Interestingly, the shoulder-like feature, occurring right after the power-law dominated region ($Q <$ ca. 0.03 Å^{-1}), is not present only in the scattering data from the extrudate soaked in 42.5% D_2O (expected contrast between cellulose and water) (Fig. 5D) (note that the shoulder shifts to the slightly lower Q-values after the soaking (Fig. S2), which might be attributed to swelling by the water). These findings suggest that the shoulder, observed within the Q range between ca. 0.01 and 0.08 Å^{-1}, can be attributed to proteins. This seems to be in line with the observation of a more pronounced shoulder in the scattering data from SPI dough (Fig. S1), where the scattering contrast arises primarily from the SLD difference of soy proteins relative to water. Although a similar shoulder feature was previously reported for bacterial cellulose (Martínez-Sanz, Lopez-Sanchez, Gidley, & Gilbert, 2015), these features were not observed in SAS data from plant cell walls (Fernandes et al., 2011; Penttilä et al., 2021). As described in (Martínez-Sanz, Gidley, & Gilbert, 2016), such a difference in scattering patterns from bacterial cellulose and plant cell wall systems is due to the presence of core-shell-like regions with distinct SLD values in the structure of bacterial cellulose. These core-shell-like regions with different solvent accessibility and distinct SLD values are the result of several cellulose microfibrils interacting via multiple hydrogen bonds within cellulose ribbons (Martínez-Sanz, Lopez-Sanchez, et al., 2015). In plant cell wall systems, cellulose microfibrils are embedded in a matrix of pectic and hemicellulosic polysaccharides (Sandhu, Randhawa, & Dhugga, 2009). Therefore, the formation of interfibrillar hydrogen bonds might be inhibited by these matrix components directly interacting with the cellulose microfibrils, leading to no core-shell regions with distinct SLD values (Martínez-Sanz et al., 2016). Curiously, the 42.5% D_2O extrudate is also the only sample that does not have an anisotropic neutron scattering response (Fig. 5D), while others show the alignment in the extrusion direction (Fig. 5A–C). The apparent differences between the degree of alignment in the samples that were unsoaked and soaked in 100% D_2O and 35% D_2O are due to different overall contrasts. Thus, these results suggest that in the extruded samples, protein structures are aligned with the extrusion direction at the length scales above ca. 13 nm ($2\pi/Q_{trans}$). In contrast, polysaccharide fibres have a more random orientation at the probed length scales.

It should be noted, however, that even though the use of contrast-matching SANS for SPC systems was confirmed to be useful to see some structural differences, it is hard to make any definitive conclusions based on these results. The main concern that has to be taken into account when interpreting contrast variation results is the possible H/D exchange of hydrogens in proteins and/or cellulose with deuterium in D_2O (Rubinson, Stanley, & Krueger, 2008). The ability of proteins to exchange backbone amide hydrogens and some side-chain hydrogens may cause the theoretical SLD values (Table 1) to deviate from experimentally determined values (Efimova, Haemers, Wierczinski, Norde, & Van Well, 2007; Perkins, 1986). Nevertheless, experimentally

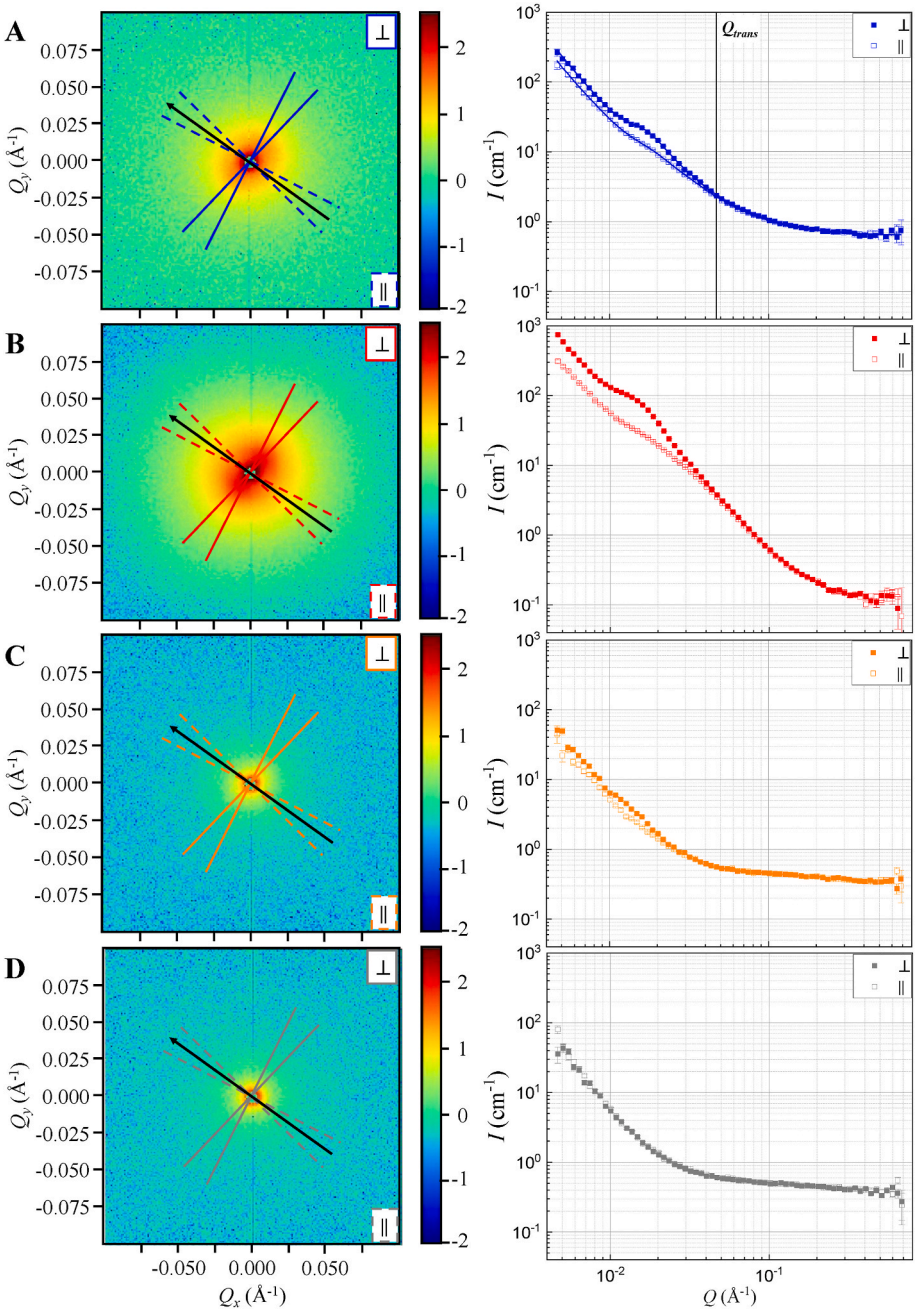

Fig. 5. 2D SANS data (scattering intensities are on logarithmic scales) (left) and sector averages taken in the directions parallel (||) and perpendicular (⊥) to the shear (right) for extrudate skin slices: a) unsoaked, b) soaked in 100% D_2O, c) soaked in 35% D_2O, and d) soaked in 42.5% D_2O. Black arrows indicate extrusion direction. Lines in a) (right) represent the fit with the broad peak model to the 100% H_2O extrudate SANS data.

determined match points for proteins fall between 39% D_2O and 45% D_2O, with many clustered in the 41–43% range (Perkins, 1986). The deviation of the theoretical SLDs from experimentally determined values was also demonstrated for cellulose (Martínez-Sanz et al., 2016). The H/D exchange undergone by the labile cellulose hydroxyl groups when cellulosic samples are soaked in H_2O/D_2O was determined to be responsible for this deviation. Taking into account the aforementioned reasons and the need to ensure the most realistic food-grade samples, the results below are presented only based on 'natural' contrast SANS experiments.

3.1.2. *Protein aggregation behaviour*

To investigate protein aggregation behaviour during HME, the experimental radially averaged data corresponding to the SPC dough in 100% H_2O and sector averages corresponding to the unsoaked dead-stops were fitted with the broad peak model (Equation (2)). The model provided a good fit along the entire Q range and reproduced the shoulder feature (examples of the fit are shown in Figs. 4 and 5A (right)). For sector averages, simultaneous fitting (with fitting parameters constrained to be equal for both parallel and perpendicular directions) significantly reduced fit quality as indicated by χ^2 increased from ca. 1 (for separate fitting) to ca. 30–40 (for simultaneous fitting) (Table S2), clearly indicating anisotropic nature of extruded SPC dough.

Although the empirical nature of the broad peak model somewhat hinders the physical interpretation of the data, the fit still provides an average centre-to-centre distance (D) between scattering inhomogeneities (all other fitting parameters are presented in Table S2). As evident from Fig. 6, D seems to change drastically when the dough

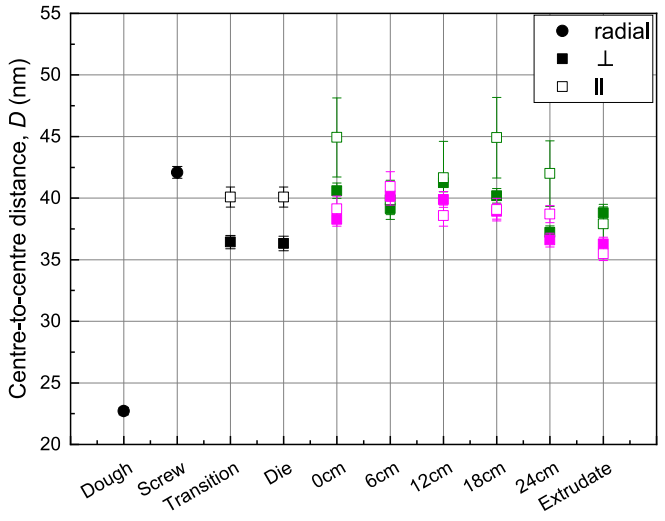

Fig. 6. Centre-to-centre distances between scattering inhomogeneities estimated from the broad peak model for the dough in 100% H_2O, unsoaked dead-stops and extrudate. Green and magenta symbols represent skin and core slices, respectively. Note that since the 2D SANS data from the dough and screw samples displayed no anisotropy, radially averaged intensities were fitted with the model. For the other dead-stop and extrudate samples, sector intensities were used for the fit.

gets subjected to the thermo-mechanical treatment in the extruder. At the same time, it remains roughly unchanged along the extruder and the entire cooling die in both perpendicular (⊥) and parallel (||) directions. This seems to agree with existing hypotheses on protein aggregation mechanisms during HME. Soy proteins have a strong tendency to self-assemble into aggregates due to the high content of sulfhydryl (SH) and disulfide (SS) groups (Hou et al., 2022). In the conditions of high moisture content, and also given the fact that the proteins present in the commercial SPC powders are already (partially) denatured via pre-processing (van der Sman & van der Goot, 2023), a facilitated aggregation might be expected in the dough even when the thermal treatment is not applied yet. At the next stage, the dough is subjected to thermo-mechanical treatment through the simultaneous application of heat and shear at elevated pressure. At the temperature above the denaturation temperature, extensive SH/SS exchange takes place, which promotes the formation of inter-molecular crosslinks, partially at the expense of intra-molecular crosslinks (Morel, Redl, & Guilbert, 2002; Osen, Toelstede, Eisner, & Schweiggert-Weisz, 2015; van der Sman & van der Goot, 2023). Additional application of shear is deemed essential to promote aggregation via lowering the activation energy (Sharma & Pandey, 2021). This increase in aggregation causes the shoulder to shift to the lower *Q*. According to (Wolz, Mersch, & Kulozik, 2016), the further change in aggregate sizes is limited by the balance between the aggregate growth and shear-induced fragmentation at the end of the screw section. This balance, which could also be expressed by the balance between thermal and mechanical (shear) energy, determines the size of protein aggregates that comprise the building blocks of the protein fibrils (van der Sman & van der Goot, 2023). Apparently, this is a reason for fairly constant *D* values along the extruder and the cooling die zones.

3.1.3. *Evolution of protein nanostructural anisotropy*

As described in (van der Sman & van der Goot, 2023), the formation of protein fibres during HME is preceded by the alignment of protein aggregates at the nanoscale. Therefore, it is essential to investigate the evolution of protein nanostructural anisotropy during shear processing. This can be done by fitting annular intensity averages with the Legendre series expansion (Equation (3)) and calculating the nematic order parameter, as explained in subsubsection 2.4.3. Fig. S3 gives an example of the goodness of the fit. Fig. 7 displays the calculated values of the nematic order parameter. Despite the small values of the order parameter characteristic for amorphous biopolymer materials with the weak alignment of nanostructural domains (Edwards, Mai, Tang, & Olsen, 2020), a significant (statistical) difference in the values of the nematic order parameter (see also Fig. S3 for comparison of annular intensities) makes it possible to clearly observe the nanoanisotropy development along the extruder and the entire cooling die section at length scales of ca. 13–125 nm.

The formation of the anisotropic structure already in the transition zone is in agreement with the results reported in other studies. For example, in (Yao, Liu, & Hsieh, 2004), similar dead-stop trials were performed to study fibre formation during the HME of soy protein isolate. There, it was also demonstrated that the anisotropic structure formation takes place in the transition zone (i.e. right after the screw section).

Further nanoanisotropy development is observed as the material progresses from the extruder barrel to the cooling die. From a comparison of skin and core slices, the extent of alignment is stronger in the skin. The large temperature gradient between the cold exterior and warm interior may account for this difference. Due to the lower temperature in the skin compared to the core, a higher viscosity is achieved in the former. In combination with the high shear stresses near the wall, one would expect a more pronounced alignment in the skin. The difference in the extent of alignment observed between skin and core at the nanoscale is also reflected at the macroscale, as seen in Fig. S4. This further confirms the sensitivity of SANS to changes in nanoanisotropy during HME.

The extent of alignment of protein fibrils slightly decreases in the extrudate compared to the cooling die ribbons. This becomes more obvious for the SPI dead-stop (Fig. S5). The expansion that perturbs the structure of the ribbon, leaving the cooling die, is the most likely reason for such a decrease. Although this expansion is minimised in the case of HME by lowering the temperature of the hot mass below the boiling temperature, some studies have still observed a decrease in the anisotropy index as the material transitions from the cooling die to atmospheric pressure (Yao et al., 2004).

3.2. *(Ultra-)Small-angle X-ray scattering ((U)SAXS)*

As described in subsection 2.5, SAXS and USAXS measurements were carried out with a beam of 100 × 150 μm^2 (v x h), which allowed local

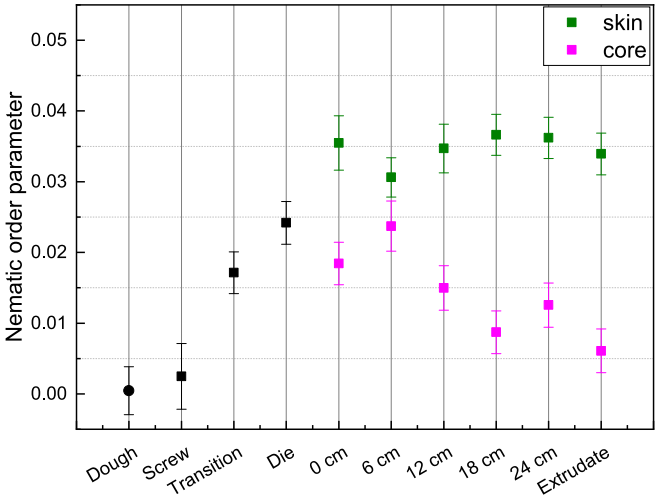

Fig. 7. Nematic order parameter, calculated from SANS data, demonstrating nanoanisotropy evolution at length scales of ca. 13–125 nm. Note that in SANS, the greater contribution to scattering is due to proteins.

examinations of 20 different sample spots over a range of 8 mm. Due to material heterogeneity, SAXS and USAXS patterns display different degrees of alignment at different sample spots. Examples of orientation angles and the order parameters determined for different spots on the skin extrudate sample are presented in Fig. S6. In order to account for material heterogeneity, averaged scattering data were obtained according to the scheme shown in Fig. 3. The resulting scattering profiles are displayed in Fig. 8.

As for the SANS data, a shoulder-like feature is evident in the Q range between ca. 0.01 and 0.05 $Å^{-1}$ (this characteristic feature is more apparent on a Kratky plot). However, it is less defined compared to the SANS data obtained with a 'natural' contrast (Fig. 5B). Table 1 indicates that X-rays exhibit lower sensitivity towards proteins when compared to neutrons. Given that the feature in the Q range between ca. 0.01 and 0.08 $Å^{-1}$ is attributed to proteins (subsubsection 3.1.1), it is anticipated that SAXS measurements would reveal a less distinct shoulder. In the lower Q region, which was not achievable with SANS ($Q < 0.005$ $Å^{-1}$), the presence of additional shoulder features is detected. Scattering intensities of all samples display a faint shoulder in the Q range between ca. 0.002 and 0.007 $Å^{-1}$, corresponding to real-space distances of ca. 90–315 nm. Considering the corresponding size range, the origin of this shoulder can be attributed to fibrillar structures of proteins. In Tian et al. (2020), a similar feature was detected in the low Q SANS data from the fibrous calcium caseinate. The lowest Q region ($Q < 0.001$ $Å^{-1}$) reveals

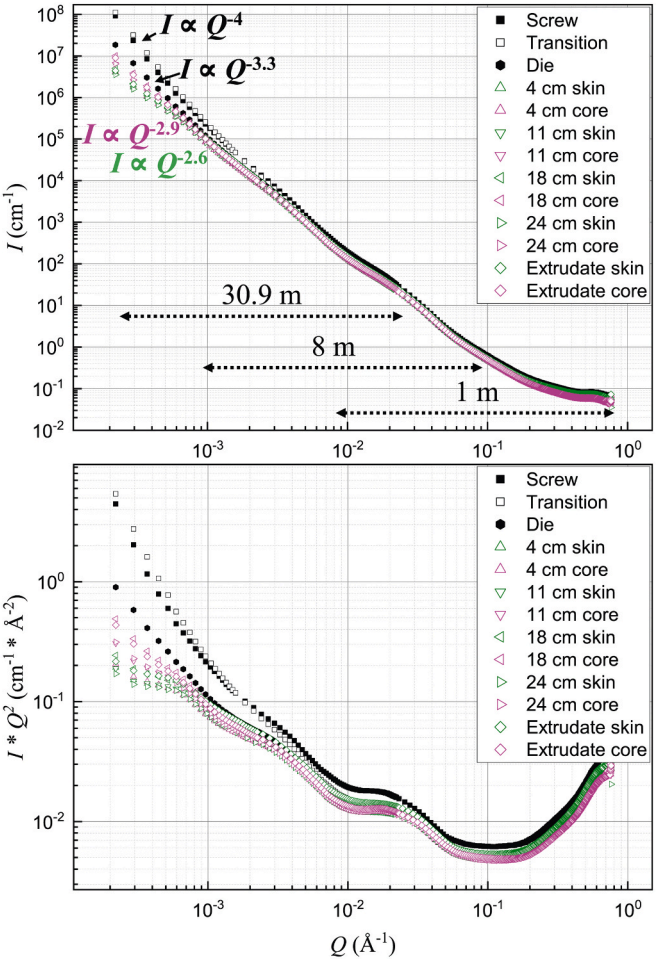

Fig. 8. Radially averaged (U)SAXS data additionally averaged over 20 measurement frames (above); corresponding Kratky plots (below). Indicated power-law coefficients were determined in the Q range 0.0002–0.002 $Å^{-1}$. Data were obtained by combining three SDDs that each covers a Q range indicated by dashed lines.

substantial differences between the micron scale structures in the extruder and cooling die samples. A decrease in the intensity of USAXS data and a decline in the power-law coefficients are observed as the material progresses from the extruder barrel to the cooling die. In the extruder barrel and non-cooled die zones, scattering intensities seem to obey the power-law. In the cooling die, the lower Q region appears to be less dominated by the power-law, and a faint shoulder-like feature becomes distinguishable. Furthermore, it is evident that scattering intensities and the power-law coefficients are lower in the skin compared to the core. Since the measured USAXS intensities are proportional to the number density of the large-scale structures, it would be reasonable to suppose that cell wall fragments are responsible for these observations. Indeed, the most clustered structures are expected to be formed in the extruder barrel due to break-up and coalescence events during intensive shearing in the extruder barrel (Tolstoguzov, 1993). Moreover, microscopy results (Fig. S7) also suggest the presence of dense regions of cotyledon tissue that have escaped much of the heating and shearing actions in the extruder barrel. As the melt passes to the cooling die, the dispersed polysaccharide fibre phase undergoes deformation and is distributed more homogeneously. The breaker plate placed before the cooling could be a reason for this. Breaker plates are known to sieve out large particulates and ensure a homogeneous pressure distribution (van der Sman & van der Goot, 2023). Since the deformation of the dispersed phase is facilitated by shear flow, it is logical to assume that the core undergoes smaller deformations compared to the skin as a result of decreased shear forces in the latter.

Surprisingly, in contrast to SANS, the nematic order parameter determined from USAXS data does not show an increase of alignment in the cooling die section (Fig. 9A). Note that since the calculated values varied significantly at different sample spots (Fig. S6), Fig. 9 A, B display the means of 20 measurement frames. Furthermore, the results suggest substantial anisotropy already in the screw section with its significant increase in the transition zone (for statistical analysis see Table S3). At the beginning of the cooling die and in the final extrudate, the probed structures appear to be non-aligned at the submicron-to-micron scale. This difference in anisotropic evolution determined from 'natural' contrast SANS and (U)SAXS data can be attributed to the different contributions of polysaccharide fibres to the scattering intensities of neutrons and X-rays, respectively. Although it is impossible to separate the contributions of proteins and polysaccharides completely, it is still evident that cellulose makes a larger contribution to (U)SAXS compared to 'natural' contrast SANS (Table 1). It is this contribution of cellulose that appears to be responsible for the strongest local alignment observed in the transition zone. Indeed, the tensile stresses are known to have an important role in the orientation of the dispersed polysaccharide fibre phase (Wittek et al., 2021a). Given that the highest tensile stresses are generated in the transition zone, one would expect the most pronounced local alignment of polysaccharide fibres there. Furthermore, the presence of more clustered or densely packed fibres in the extruder section may also add to the observation of substantial local alignment in the extruder barrel. The apparent lack of polysaccharide fibre alignment in the final extrudate would be in line then with the isotropic SANS data from the extrudate, soaked in 42.5% D_2O, for which the scattering signal is anticipated to be due to the contrast between polysaccharide fibres and water (Fig. 5D). The expansion of the ribbon upon leaving the cooling die could be the reason for this observation.

As evident from Fig. 9B, the alignment of cell wall fragments occurs along with the flow in both extruder and cooling die sections. Curiously, even though there is no significant difference between order parameters in the skin and core slices collected from the cooling die, it is clear that standard deviations in orientation angles are larger for the core. The differences between the skin and core are in line with the SANS data that showed weaker alignment in the core compared to the skin determined for a large sample area of 6 × 6 mm^2 (Fig. 7). A large standard deviation in the non-cooled die zone does not imply a random orientation of the fibres, but, on the contrary, accurately describes the orientation with the

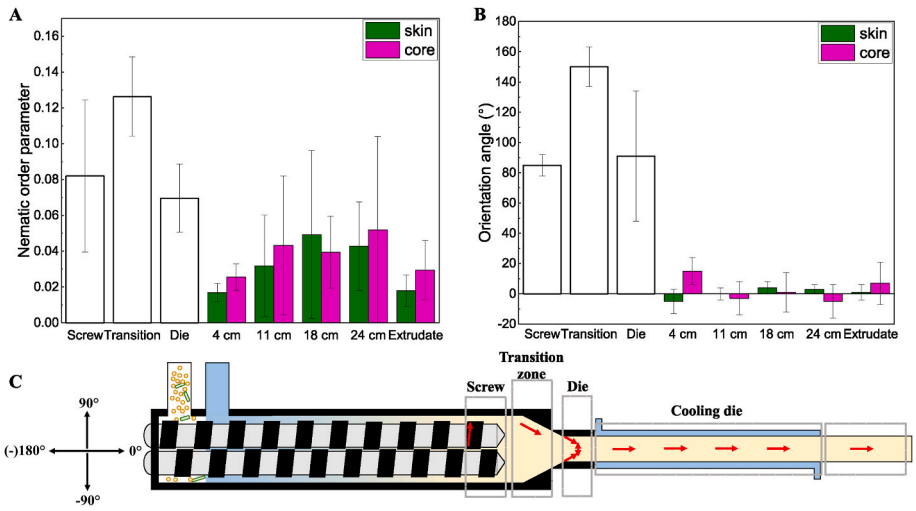

Fig. 9. Nano- and microstructure evolution during HME demonstrated by nematic order parameters (A) and orientation angles (B), calculated from (U)SAXS data at SDD of 31 m, i.e. at length scales of ca. 30 nm - 3 μm. Note that, in (U)SAXS, contribution of polysaccharide fibres is greater when compared to SANS. Results are the means of 20 measurement frames. The calculated error bars are the result of strong heterogeneity and the existence of regions with varying alignment within the samples. A schematic diagram of fibre orientation is presented in (C).

flow, as schematically shown in Figure Fig. 9C.

4. Conclusions

The complementary use of SANS and SAXS has been demonstrated to be a powerful strategy for studying the role of both proteins and polysaccharide fibres in the anisotropic structure formation at the nano- and submicron scale. The data collected provide evidence that two biopolymers have differences in the development of anisotropy.

Considering the greater contribution of proteins to the SANS signal, it has been shown that, in the screw section, protein aggregates grow (Fig. 10 (1 → 2)) until reaching the size that remains the same in the subsequent extruder and cooling die sections (Fig. 10 (2 → 5)). These protein aggregates of stable size probably constitute the building blocks of the protein fibrils. The transition section (Fig. 10 (3)) has demonstrated the presence of protein fibril alignment, which continues to evolve as the dough progresses through the die (Fig. 10 (3 → 5)). Due to the temperature gradient in the cooling die (Fig. 10 (5)), the alignment extent gradually increases from the warm core to the cold exterior (Fig. 10 (5, 6: skin vs core)). Upon exiting the cooling die (Fig. 10 (6)), the extent of alignment of protein fibrils slightly decreases, which is likely due to the expansion of the extruded material.

The fact that polysaccharide fibres make a greater contribution to the SAXS signal compared to the 'natural' contrast SANS has enabled the investigation of the role of the second dispersed biopolymeric phase in the anisotropic structure formation. In contrast to proteins, the substantial alignment of highly clustered and/or densely packed cell wall fragments has been observed already in the screw section (Fig. 10 (2)). Probably due to the highest tensile stresses expected in the transition zone, this zone demonstrates a significantly stronger preferred orientation of polysaccharide fibres (Fig. 10 (3)) compared to the non-cooled and cooling die zones (Fig. 10 (4,5)). In the final extrudate (Fig. 10 (6)), cell wall fragments appear to be non-aligned at the submicron-to-micron scale, which is likely due to the expansion of the extruded material.

CRediT authorship contribution statement

Ekaterina D. Garina: Writing – original draft, Visualization, Methodology, Investigation, Formal analysis, Data curation, Conceptualization. **Ruud den Adel:** Methodology, Conceptualization. **John P.M. van Duynhoven:** Writing – review & editing, Supervision, Resources,

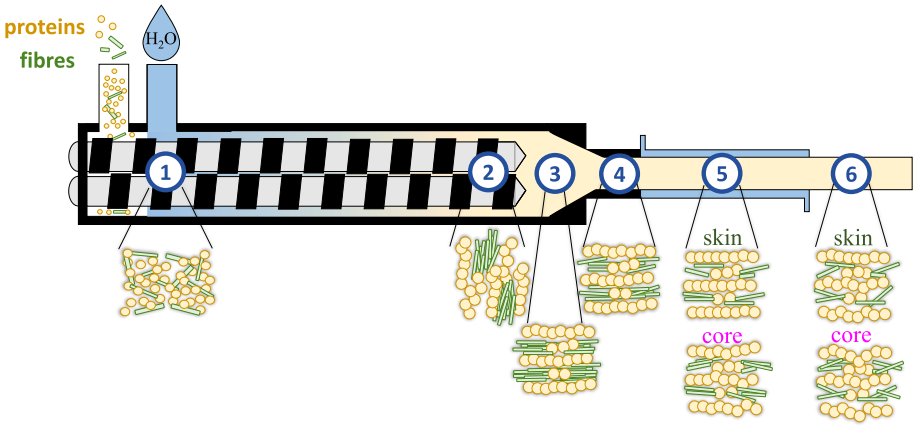

Fig. 10. Schematic diagram reflecting the hypothesis of the structural evolution of protein fibrils and polysaccharide fibres during HME. Note that the figure is not to scale. Proteins and polysaccharide fibres are on different scales (protein fibril and polysaccharide fibre alignments were determined from SANS and USAXS data at the length scales of ca. 13–125 nm and ca. 30 nm - 3 μm, respectively).

Funding acquisition. **Gregory N. Smith:** Software, Data curation. **Robert M. Dalgliesh:** Software, Data curation. **Michael Sztucki:** Software, Data curation. **Wim G. Bouwman:** Writing – review & editing, Supervision, Methodology, Funding acquisition.

Declaration of competing interest

John P.M. van Duynhoven and Ruud den Adel are employed by a company that manufactures and markets plant-based meat alternatives. The other authors declare that they have no known competing financial interests or personal relationships that could have appeared to influence the work reported in this paper.

Data availability

SANS data are available at doi.org/10.5286/ISIS.E.RB2269101. (U) SAXS data are available at doi.org/10.15151/ESRF-DC-1443749474.

Effects of pH and salt concentration on the fibrous structure formation of plant proteins during high-moisture extrusion and shear (Original data) (ISIS)

Structure formation and structure evolution during high moisture extrusion of soy proteins (Original data) (ESRF)

Acknowledgements

This work is part of the project "Measurement and Modelling of Multiscale Processed Protein Products (MP3)" (with project number 18744) of the research programme OPT TTW, which is financed by the Dutch Research Council as well as contributions from consortium partners Unilever, Cargill, dsm-firmenich, FrieslandCampina and Wageningen Food and Biobased Research.

We gratefully acknowledge the Science and Technology Facilities Council (STFC) for access to neutron beamtime at ISIS through RB 2269101 (data are available at https://doi.org/10.5286/ISIS.E.RB2269101).

We also acknowledge the European Synchrotron Radiation Facility (ESRF) for the provision of synchrotron radiation facilities (data are available at https://doi.org/10.15151/ESRF-DC-1443749474).

We acknowledge the support of the Hoger Onderwijs Reactor (HOR) in providing access to FISH, a thermal neutron imaging station.

This work benefited from the use of the SasView application, originally developed under NSF Award DMR-0520547. SasView also contains code developed with funding from the EU Horizon 2020 programme under the SINE2020 project Grant No 654000.

Finally, we thank Kalyan Panda for performing extrusion trials, Stan Zaalberg - for helping with sample preparation, Martijn Gobes - for providing CLSM images for supplementary materials, Sam Kuijpers - for providing MRI images for supplementary materials, and Yueer Li and Sterre van der Wal - for carrying out neutron radiography at FISH.

Appendix A. Supplementary data

Supplementary data to this article can be found online at https://doi.org/10.1016/j.foodhyd.2024.110121.

References

Aiking, H., & de Boer, J. (2020). The next protein transition. *Trends in Food Science & Technology, 105*, 515–522. https://doi.org/10.1016/j.tifs.2018.07.008

Akdogan, H. (1999). High moisture food extrusion. *International Journal of Food Science and Technology, 34*, 195–207. https://doi.org/10.1046/j.1365-2621.1999.00256.x

Arnold, O., Bilheux, J. C., Borreguero, J. M., Buts, A., Campbell, S. I., Chapon, L., et al. (2014). Mantid - data analysis and visualization package for neutron scattering and μ SR experiments. *Nuclear Instruments and Methods in Physics Research Section A: Accelerators, Spectrometers, Detectors and Associated Equipment, 764*, 156–166. https://doi.org/10.1016/j.nima.2014.07.029

Burger, C., Hsiao, B. S., & Chu, B. (2010). Preferred orientation in polymer fiber scattering. *Polymer Reviews, 50*, 91–111. https://doi.org/10.1080/15583720903503494

ChemSrc. https://www.chemsrc.com/en/cas/9010-10-0_1198690.html. (Accessed 19 February 2024).

Collier, E. S., Oberrauter, L. M., Normann, A., Norman, C., Svensson, M., Niimi, J., et al. (2021). Identifying barriers to decreasing meat consumption and increasing acceptance of meat substitutes among Swedish consumers. *Appetite, 167*, Article 105643. https://doi.org/10.1016/j.appet.2021.105643

Cornet, S. H., Snel, S. J., Lesschen, J., van der Goot, A. J., & van der Sman, R. G. (2021). Enhancing the water holding capacity of model meat analogues through marinade composition. *Journal of Food Engineering, 290*, Article 110283. https://doi.org/10.1016/j.jfoodeng.2020.110283

Cornet, S. H., Snel, S. J., Schreuders, F. K., van der Sman, R. G., Beyrer, M., & van der Goot, A. J. (2022). Thermo-mechanical processing of plant proteins using shear cell and high-moisture extrusion cooking. *Critical Reviews in Food Science and Nutrition, 62*, 3264–3280. https://doi.org/10.1080/10408398.2020.1864618

Doucet, M., Cho, J. H., Alina, G., Attala, Z., Bakker, J., Bouwman, W., et al. (2022). *SasView version 5.0.5*. https://doi.org/10.5281/zenodo.6331344

Edwards, C. E., Mai, D. J., Tang, S., & Olsen, B. D. (2020). Molecular anisotropy and rearrangement as mechanisms of toughness and extensibility in entangled physical gels. *Physical Review Materials, 4*, Article 015602. https://doi.org/10.1103/PhysRevMaterials.4.015602

Efimova, Y. M., Haemers, S., Wierczinski, B., Norde, W., & Van Well, A. A. (2007). Stability of globular proteins in H2O and D2O. *Biopolymers, 85*, 264–273. https://doi.org/10.1002/BIP.20645

Emin, M. A., & Schuchmann, H. P. (2017). A mechanistic approach to analyze extrusion processing of biopolymers by numerical, rheological, and optical methods. *Trends in Food Science & Technology, 60*, 88–95. https://doi.org/10.1016/j.tifs.2016.10.003

Fernandes, A. N., Thomas, L. H., Altaner, C. M., Callow, P., Forsyth, V. T., Apperley, D. C., et al. (2011). Nanostructure of cellulose microfibrils in spruce wood. *Proceedings of the National Academy of Sciences of the United States of America, 108*, E1195–E1203. https://doi.org/10.1073/pnas.1108942108

Goh, K. L., Hiller, J., Haston, J. L., Holmes, D. F., Kadler, K. E., Murdoch, A., et al. (2005). Analysis of collagen fibril diameter distribution in connective tissues using small-angle X-ray scattering. *Biochimica et Biophysica Acta (BBA) - General Subjects, 1722*, 183–188. https://doi.org/10.1016/j.bbagen.2004.12.004

Guyony, V., Fayolle, F., & Jury, V. (2023). High moisture extrusion of vegetable proteins for making fibrous meat analogs: A review. *Food Reviews International, 39*, 4262–4287. https://doi.org/10.1080/87559129.2021.2023816

Hammouda, B. (2010). A new Guinier-Porod model. *Journal of Applied Crystallography, 43*, 716–719. https://doi.org/10.1107/S0021889810015773

Hou, Y., Yang, F., Cao, J., Huang, Y., Li, C., Li, J., et al. (2022). Effects of hydrodynamic cavitation at different pH values on the physicochemical properties and aggregation behavior of soybean glycinin. *Lebensmittel-Wissenschaft und -Technologie, 163*, Article 113615. https://doi.org/10.1016/j.lwt.2022.113615

ISIS Larmor. https://www.isis.stfc.ac.uk/Pages/Larmor.aspx. (Accessed 21 July 2023).

Levenberg, K. (1944). A method for the solution of certain non-linear problems in least squares. *Quarterly of Applied Mathematics, 2*, 164–168. https://doi.org/10.1090/QAM2F10666

Marquardt, D. W. (1963). An algorithm for least-squares estimation of nonlinear parameters. *Journal of the Society for Industrial and Applied Mathematics, 11*, 431–441. https://doi.org/10.1137/0111030

Martínez-Sanz, M., Gidley, M. J., & Gilbert, E. P. (2015a). Application of X-ray and neutron small angle scattering techniques to study the hierarchical structure of plant cell walls: A review. *Carbohydrate Polymers, 125*, 120–134. https://doi.org/10.1016/j.carbpol.2015.02.010

Martínez-Sanz, M., Gidley, M. J., & Gilbert, E. P. (2016). Hierarchical architecture of bacterial cellulose and composite plant cell wall polysaccharide hydrogels using small angle neutron scattering. *Soft Matter, 12*, 1534–1549. https://doi.org/10.1039/c5sm02085a

Martínez-Sanz, M., Lopez-Sanchez, P., Gidley, M. J., & Gilbert, E. P. (2015b). Evidence for differential interaction mechanism of plant cell wall matrix polysaccharides in hierarchically-structured bacterial cellulose. *Cellulose, 22*, 1541–1563. https://doi.org/10.1007/s10570-015-0614-2

Morel, M. H., Redl, A., & Guilbert, S. (2002). Mechanism of heat and shear mediated aggregation of wheat gluten protein upon mixing. *Biomacromolecules, 3*, 488–497. https://doi.org/10.1021/bm015639p

Narayanan, T., Sztucki, M., Zinn, T., Kieffer, J., Homs-Puron, A., Gorini, J., et al. (2022). Performance of the time-resolved ultra-small-angle X-ray scattering beamline with the Extremely Brilliant Source. *Journal of Applied Crystallography, 55*, 98–111. https://doi.org/10.1107/S1600576721012693

NIST. https://www.ncnr.nist.gov/resources/sldcalc.html. (Accessed 19 February 2024).

Osen, R., Toelstede, S., Eisner, P., & Schweiggert-Weisz, U. (2015). Effect of high moisture extrusion cooking on protein–protein interactions of pea (Pisum sativum L.) protein isolates. *International Journal of Food Science and Technology, 50*, 1390–1396. https://doi.org/10.1111/ijfs.12783

Osen, R., Toelstede, S., Wild, F., Eisner, P., & Schweiggert-Weisz, U. (2014). High moisture extrusion cooking of pea protein isolates: Raw material characteristics, extruder responses, and texture properties. *Journal of Food Engineering, 127*, 67–74. https://doi.org/10.1016/j.jfoodeng.2013.11.023

Penttilä, P. A., Zitting, A., Lourençon, T., Altgen, M., Schweins, R., & Rautkari, L. (2021). Water-accessibility of interfibrillar spaces in spruce wood cell walls. *Cellulose, 28*, 11231–11245. https://doi.org/10.1007/s10570-021-04253-3

Perkins, S. J. (1986). Protein volumes and hydration effects. The calculations of partial specific volumes, neutron scattering matchpoints and 280-nm absorption coefficients

for proteins and glycoproteins from amino acid sequences. *European Journal of Biochemistry, 157*, 169–180. https://doi.org/10.1111/j.1432-1033.1986.tb09653.X

Pette, D., & Staron, R. S. (1990). Cellular and molecular diversities of mammalian skeletal muscle fibers. *Reviews of Physiology, Biochemistry & Pharmacology, 116*, 1–76. https://doi.org/10.1007/3540528806_3

Rubinson, K. A., Stanley, C., & Krueger, S. (2008). Small-angle neutron scattering and the errors in protein structures that arise from uncorrected background and intermolecular interactions. *Journal of Applied Crystallography, 41*, 456–465. https://doi.org/10.1107/S0021889808004950

Sandhu, A. P. S., Randhawa, G. S., & Dhugga, K. S. (2009). Plant cell wall matrix polysaccharide biosynthesis. *Molecular Plant, 2*, 840–850. https://doi.org/10.1093/mp/ssp056

Schmid, E. M., Farahnaky, A., Adhikari, B., & Torley, P. J. (2022). High moisture extrusion cooking of meat analogs: A review of mechanisms of protein texturization. *Comprehensive Reviews in Food Science and Food Safety, 21*, 4573–4609. https://doi.org/10.1111/1541-4337.13030

Sharma, L. G., & Pandey, L. M. (2021). Thermomechanical process induces unfolding and fibrillation of bovine serum albumin. *Food Hydrocolloids, 112*, Article 106294. https://doi.org/10.1016/j.foodhyd.2020.106294

Sztucki, M. (2021). *SAXSutilities: A graphical user interface for processing and analysis of small-angle X-ray scattering data (1.024)*. https://doi.org/10.5281/zenodo.5825707

Tian, B., Wang, Z., de Campo, L., Gilbert, E. P., Dalgliesh, R. M., Velichko, E., et al. (2020). Small angle neutron scattering quantifies the hierarchical structure in fibrous calcium caseinate. *Food Hydrocolloids, 106*, Article 105912. https://doi.org/10.1016/j.foodhyd.2020.105912

Tolstoguzov, V. B. (1993). Thermoplastic extrusion—the mechanism of the formation of extrudate structure and properties. *Journal of the American Oil Chemists' Society, 70*, 417–424. https://doi.org/10.1007/BF02552717

Ubbink, J., & Muhialdin, B. J. (2022). Protein physical state in meat analogue processing. *Current Opinion in Food Science, 45*, Article 100822. https://doi.org/10.1016/j.cofs.2022.100822

van den Berg, S. W., van den Brink, A. C., Wagemakers, A., & den Broeder, L. (2022). Reducing meat consumption: The influence of life course transitions, barriers and enablers, and effective strategies according to young Dutch adults. *Food Quality and Preference, 100*, Article 104623. https://doi.org/10.1016/j.foodqual.2022.104623

van der Sman, R. G., & van der Goot, A. J. (2023). Hypotheses concerning structuring of extruded meat analogs. *Current Research in Food Science, 6*, Article 100510. https://doi.org/10.1016/j.crfs.2023.100510

Wignall, G. D., & Bates, F. S. (1987). Absolute calibration of small-angle neutron scattering data. *Journal of Applied Crystallography, 20*, 28–40. https://doi.org/10.1107/S0021889887087181

Wittek, P., Ellwanger, F., Karbstein, H. P., & Emin, M. A. (2021a). Morphology development and flow characteristics during high moisture extrusion of a plant-based meat analogue. *Foods, 10*. https://doi.org/10.3390/foods10081753

Wittek, P., Zeiler, N., Karbstein, H. P., & Emin, M. A. (2021b). High moisture extrusion of soy protein: Investigations on the formation of anisotropic product structure. *Foods, 10*. https://doi.org/10.3390/foods10010102

Wittek, P., Zeiler, N., Karbstein, H. P., & Emin, M. A. (2021c). High moisture extrusion of soy protein: Investigations on the Formation of anisotropic product structure. *Foods, 10*, 102. https://doi.org/10.3390/foods10010102, 2021, Vol. 10, Page 102.

Wolz, M., Mersch, E., & Kulozik, U. (2016). Thermal aggregation of whey proteins under shear stress. *Food Hydrocolloids, 56*, 396–404. https://doi.org/10.1016/j.foodhyd.2015.12.036

Yao, G., Liu, K. S., & Hsieh, F. (2004). A new method for characterizing fiber formation in meat analogs during high-moisture extrusion. *Journal of Food Science, 69*, 303–307. https://doi.org/10.1111/j.1365-2621.2004.tb13634.x

Zhou, Z., Plomp, J., van Eijck, L., Vontobel, P., Harti, R. P., Lehmann, E., et al. (2018). FISH: A thermal neutron imaging station at HOR Delft. *Journal of Archaeological Science: Report, 20*, 369–373. https://doi.org/10.1016/j.jasrep.2018.05.015

Zink, J. I., Lutz-Bueno, V., Handschin, S., Dütsch, C., Diaz, A., Fischer, P., et al. (2024). Structural and mechanical anisotropy in plant-based meat analogues. *Food Research International, 179*, Article 113968. https://doi.org/10.1016/j.foodres.2024.113968